Faraday Discussions

Cite this: *Faraday Discuss.*, 2018, **210**, 173

PAPER

Electrochemistry at a single nanoparticle: from bipolar regime to tunnelling

Tong Sun,[ab] Dengchao Wang[a] and Michael V. Mirkin *[ab]

Received 19th February 2018, Accepted 29th March 2018
DOI: 10.1039/c8fd00041g

This paper is concerned with long-distance interactions between an unbiased metal nanoparticle (NP) and a nanoelectrode employed as a tip in the scanning electrochemical microscope (SECM). A NP immobilized on the inert substrate acts as a bipolar electrode, producing positive SECM feedback. The tip current magnitude depends strongly on the ratio of the particle and tip radii and the heterogeneous charge-transfer kinetics. The onset of electron tunneling was observed at very short separation distances (<2–3 nm) at which the NP behaves as a part of the tip electrode. The rate constant of the electron-transfer (ET) or electrocatalytic reaction at the NP can be extracted from either feedback or tunneling current. The tunneling mode of SECM can be used to investigate heterogeneous reactions occurring at a single NP without making an ohmic contact with it. This technique can also help elucidate nanoparticle/electrode interactions in various electrochemical systems ranging from NPs immobilized on the electrode surface to nanoimpact collision events.

Introduction

Nanomaterial-based electrochemical systems have attracted considerable attention due to their technological and biomedical applications.[1–4] Different ways of coupling nanoobjects to electrodes range from nanomaterial-based films, in which nanometer-sized building blocks, *e.g.*, nanoparticles (NP), nanorods and 2D nanosheets, are attached to the electrode surface, to single entity collisions of nanoobjects dispersed in solution with the collector electrode. In both cases an essential issue is the long-distance interactions between the electrode and conductive nanoparticles.[5–7] In most cases, a NP is separated from the electrode surface by some distance determined either by the capping layer thickness or the thickness of the molecular film deposited on the electrode for NP attachment,[8] or that of the passivating layer.[5] It was previously shown that electron tunnelling between the electrode surface and a NP can occur over a distance (d) of a few nm.[9]

[a]*Department of Chemistry and Biochemistry, Queens College-CUNY, Flushing, New York 11367, USA. E-mail: mmirkin@qc.cuny.edi*
[b]*The Graduate Center of CUNY, New York, NY 10016, USA*

For small NPs, the distance corresponding to the onset of tunnelling increases with the particle radius (r_p).[10]

Microscopic understanding of electron tunneling between metal NPs and electrodes is essential for rational design of nanostructured interfaces for sensing and electrocatalysis. However, measuring and especially varying the molecular scale NP/electrode distance and the NP potential is not straightforward.[5] Similarly, the time variation of the separation distance during the NP collision with the electrode surface is not known, and the shape of the collision transient was modeled assuming the "binary nature" of electron transfer, *i.e.* the current switching between zero and the limiting faradaic current when the NP touches the surface.[11]

We showed recently that the separation distance can be varied and controlled on the nanoscale by using a nanoelectrode as a tip in the scanning electrochemical microscope (SECM) to approach an immobilized 10–100 nm NP.[12] The metal NPs were immobilized on a flat electrochemically inert surface, which provided an electrical connection to the particles. In a feedback mode experiment, a nm-sized SECM probe approached a metal NP in solution containing redox mediator (*e.g.*, a reduced form *R*; Fig. 1a), and the tip potential (E_T) was such that the mediator oxidation occured at the rate governed by diffusion. With the NP potential (E_P) determined either by externally applied bias or by the open-circuit potential of the underlying macroscopic substrate, the oxidized form of the mediator produced at the tip surface was reduced at the NP surface when the separation distance (d) became comparable to the tip radius (a). The tip current (i_T) increased with decreasing d (positive feedback).

Unlike SECM experiments in ref. 12, in this paper, Au NPs are immobilized on the insulating substrate surface (Fig. 1B). When the tip is relatively far from the NP (*e.g.*, >∼3–4 nm), the open-circuit NP potential is determined by the concentrations of the reduced form (*e.g.*, ferrocenemethanol, Fc; initially present in solution) and oxidized (Fc^+; electro-generated at the tip) forms of the reversible redox mediator, according to the Nernst equation. If the r_p is not much smaller than a, the NP potential can be sufficiently negative to regenerate Fc species, producing positive SECM feedback at the unbiased substrate.[13,14]

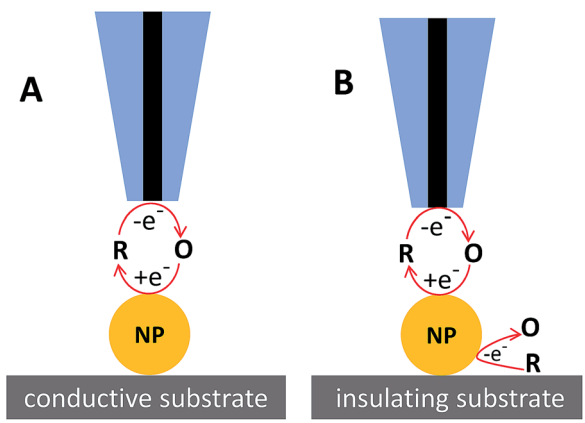

Fig. 1 Schematic representation of the SECM feedback at the externally biased metal NP (A) and bipolar feedback at the floating NP (B).

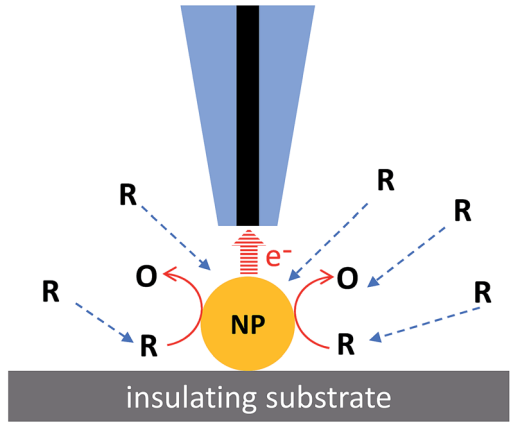

Fig. 2 SECM tunnelling experiment at a metal nanoparticle. The overall charge-transfer process involves diffusion of redox species to the NP, faradaic reaction at its surface, and electron tunnelling between the tip and NP.

The unbiased NP behaves as a bipolar electrode, with the regeneration of the redox mediator (*e.g.*, $Fc^+ + e^- = Fc$) occurring at the top half of the NP facing the tip, and the opposite reaction (*e.g.*, $Fc - e^- = Fc^+$) – at the bottom half of the NP. Here, we develop a theoretical description for the bipolar response and demonstrate the possibility of kinetic measurements at an unbiased NP.

The onset of electron tunnelling is expected when the tip approaches a NP to within $d \approx 1$–3 nm (Fig. 2).[5,9,10] When the tip is brought within the tunnelling distance from the NP, the E_P should shift from its open-circuit value toward the E_T value, and the NP is expected to act as a part of the tip electrode, *e.g.*, by oxidizing the reduced form of the mediator (Fig. 2). With no voltage applied between the tip and the substrate, the maximum i_T value in this experiment is determined by diffusion of redox species to the NP surface. Although this process has not yet been observed in SECM approach curves, the indirect evidence of the tip/NP tunneling was inferred from extremely high lateral resolution (~1 nm) in the images of Pd nanocubes.[15]

Experimental methods and simulations

Materials

Ferrocenemethanol (Fc; 99%, Sigma-Aldrich) was sublimed before use. 4-Aminobenzylamine (99%), trimethoxysilane (95%), acetonitrile (99.8%) $NaNO_2$ (99.99%), KCl (99%), $HClO_4$ (70%) and $NaClO_4$ (99%) were purchased from Sigma-Aldrich and used as received. Au NPs (Ted Pella, Inc.), were either 20 nm diameter (as specified by the vendor; 7.0×10^{11} particles per mL) or 100 nm diameter (5.6×10^9 particles per mL) and were stabilized by trace amounts of citrate. The Au–Pt bimetallic nanorods (~2 μm long and 370 nm diameter)[16] were synthesized in Prof. Michael Ward's laboratory (New York University). All aqueous solutions were prepared using ultra-pure water (18.2 MΩ cm) from the Milli-Q Advantage A10 system (Millipore) equipped with Q-Gard T2 Pak, a Quantum TEX cartridge and a VOC Pak with total organic carbon (TOC) ≤1 ppb.

Fabrication of Pt and C nanoelectrodes

Polished disk-type Pt nanoelectrodes were prepared by pulling 25 μm-diameter annealed Pt wires into borosilicate glass capillaries with a P-2000 laser pipette puller (Sutter Instrument Co.) and polishing under video microscopic control, as described previously.[17] The nanoelectrodes were characterized using AFM imaging and voltammetry.

Carbon nanoelectrodes were prepared by chemical vapor deposition of carbon inside pre-pulled quartz nanopipettes, as described previously.[18]

SECM setup and electrochemical experiments

Voltammograms were obtained with a BAS-100B electrochemical workstation (Bioanalytical Systems, West Lafayette, IN) inside a Faraday cage. The two-electrode setup was used, with a 0.25 mm diameter Ag wire coated with AgCl serving as a reference electrode. SECM experiments were carried out using a previously described home-built instrument.[19] To obtain an approach curve, the tip electrode was first positioned about 100 μm above the substrate surface. To avoid tip crashing, this process was monitored with a long-distance video microscope. Then, the tip was moved closer to the substrate in the automated "surface hunter" mode until the tip current either increased (positive feedback) or decreased (negative feedback) by ~10%. The tip current was collected during the subsequent fine approach or voltammetry. The approach velocity was either 10 nm s^{-1} (feedback mode current–distance curves) or 2 nm s^{-1} (tunneling mode current–distance curves). All experiments were carried out at room temperature (23 ± 2 °C) inside a Faraday cage. To prevent hydrogen bubble formation either at the tip or substrate electrode, the acid concentration in HER experiments was always less than 40 mM.

Immobilization of mercaptosilane-stabilized Au NPs on glass surface

The surface of a glass slide was modified with a layer of trimethoxysilane by silane chemistry, as described in the literature.[20] Briefly, after adding 1 μL trimethoxysilane to 40 mL acetonitrile, a glass slide was immersed in solution for 10 min.

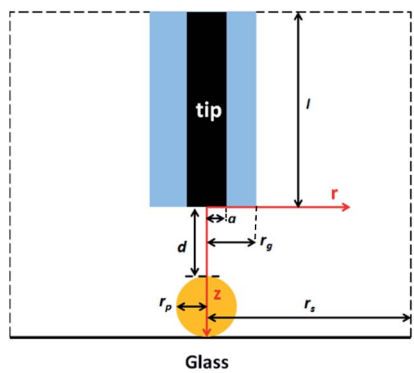

Scheme 1 Geometry of the simulation space and parameters defining the diffusion and electron tunnelling problems for the disk-shaped SECM tip approaching a spherical NP attached to the planar insulating substrate.

The coated glass surface was then rinsed with acetonitrile to remove excess trimethoxysilane. The negatively charged citrate-stabilized gold particles were then attached to the glass surface by immersing the modified glass slide in either 1 nM (20 nm NPs) or 0.1 nM (100 nm NPs) Au NP solution for 30 min.

Simulations of bipolar NP response and tip/NP tunnelling

Feedback and tunnelling mode SECM experiments at single unbiased NPs were simulated using a commercial finite-element package (COMSOL Multiphysics 5.2a; see Appendix for details of mathematical models). The geometry of the system and related parameters are shown in Scheme 1.

Results and discussion

Bipolar feedback and ET kinetics at an unbiased Au NP

The magnitude of positive SECM feedback produced by an unbiased spherical nanoparticle depends strongly on the ratio of the NP and tip radii (RP = r_p/a). A family of simulated i_T–d curves for the diffusion-controlled (Nernstian) mediator regeneration at the NP (Fig. 3A) shows a gradual transition from the negative to

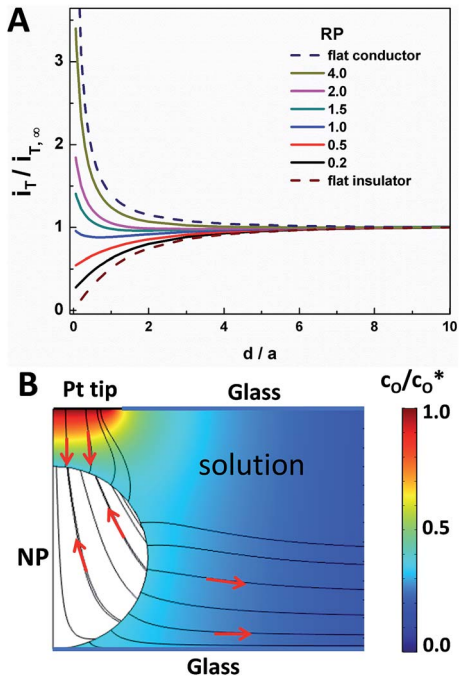

Fig. 3 (A) Simulated dimensionless i_T–d curves for the diffusion-limited feedback produced by unbiased spherical NPs with different RP values, and (B) representative 2D concentration distribution of the oxidized species. (A) Dashed curves are calculated for the pure positive (top) and negative (bottom) SECM feedback at the infinitely large flat substrate. (B) $a = 30$ nm; $r_p = 50$ nm; $d = 30$ nm; RG = $r_g/a = 10$. The thin lines and red arrows represent the flux of the oxidized species in solution and electronic current inside the NP. $E_T = E^0 + 0.3$ V. $i_{T,\infty}$ is the steady-state diffusion limiting tip current far away from the NP (see eqn (11) in Appendix).

positive feedback with increasing RP. Unlike SECM experiments at an unbiased disk-shaped substrate, where the substrate radius must be as least $\sim 10a$ to produce positive feedback,[14] the i_T in Fig. 3A increases at short d when RP ≥ 1.

The corresponding concentration and flux density distributions near the NP surface shown in Fig. 3B illustrate the bipolar behavior of the NP whose upper half regenerates the mediator, while the opposite reaction (oxidation) occurs at the lower hemisphere, resulting in the zero total current at the unbiased NP.

For the finite ET kinetics at the NP, the shape of the current–distance curve is determined by the values of RP and the kinetic parameter, $\lambda = ak^0/D$, where k^0 is the standard heterogeneous rate constant (the transfer coefficient value, $\alpha = 0.5$, was used) and D is the diffusion coefficient of the dissolved redox species. Three series of dimensionless current *vs.* distance curves simulated for different RP values and RG = 10 (RG is the ratio of glass sheath radius, r_g, to a) are shown in Fig. 4. Unlike feedback experiments at an externally biased substrate, the k^0 determines not only the ET rate, but also the E_P value. The sensitivity of the shape

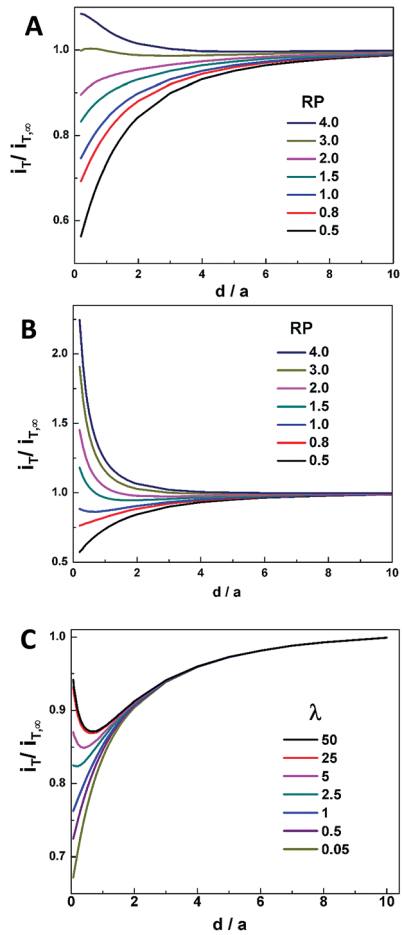

Fig. 4 Simulated dimensionless i_T–d curves for the finite kinetics at unbiased NPs at different RP and λ values. $\lambda = 0.05$ (A) and 25 (B). RP = 1 (C).

of the i_T–d curve to λ depends on the RP value. The RP values in the range from ~1 to ~1.5 are most suitable for kinetic analysis. The difference between the curves corresponding to $\lambda = 5$ (pink) and 25 (red) in Fig. 4C is more significant than that measured and simulated previously at the flat, externally biased SECM substrate.[21] This indicates that rapid heterogeneous ET kinetics can be measured at unbiased NPs.

An experimental current–distance curve in Fig. 5 (symbols) was obtained with a Pt tip (a = 30 nm) approaching 50 nm-radius Au NP attached to the glass substrate in solution containing 1 mM Fc. This curve fits well the theory for k^0 = 10 cm s^{-1} (red curve) and is bracketed by theoretical curves simulated with k^0 = 5 cm s^{-1} (blue) and 20 cm s^{-1} (green). This result is in good agreement with the rate of ferrocenemethanol oxidation previously obtained from voltammograms at Au nanoelectrodes ($k^0 = 8 \pm 1$ cm s^{-1}).[22]

Transition from bipolar regime to NP/tip electron tunnelling

Simulated data illustrating the transition from feedback mode SECM response at an unbiased metal NP to electron tunnelling is shown in Fig. 6. When d becomes ≤~2 nm, the E_P gradually shifts from its open-circuit value determined by local concentrations of redox species towards the E_T value (Fig. 6A). The corresponding sharp increase in the tip current with decreasing d (Fig. 6B) is largely determined by the decrease in the tunnelling resistance (see eqn (19) in Appendix). For a Nerstian ET process and the E_T value sufficiently extreme, the diffusion limiting plateau current in Fig. 6B is determined by RP and can be used to evaluate the NP radius.

The essential differences between the tunnelling and bipolar feedback responses can be seen by comparing the concentration and current distributions in Fig. 3B and 6C. In the latter, no mediator regeneration occurs in the tip/NP gap because both the E_P and E_T are much more positive than E^0, and nearly all mediator species in this region are oxidized. In the tunnelling regime, the NP acts

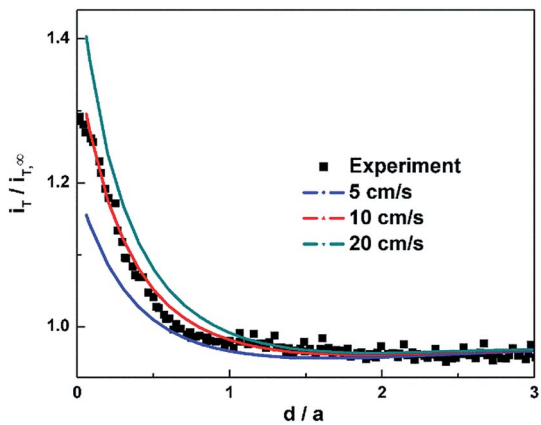

Fig. 5 Experimental current–distance curve (black squares) obtained with a Pt tip approaching an Au NP immobilized on the glass surface in solution containing 1 mM Fc and 0.1 M KCl and theoretical curves simulated for k^0, cm s^{-1} = 5 (blue), 10 (red), and 20 (green). r_p = 50 nm, a = 30 nm. E_T = 400 mV *vs.* Ag/AgCl.

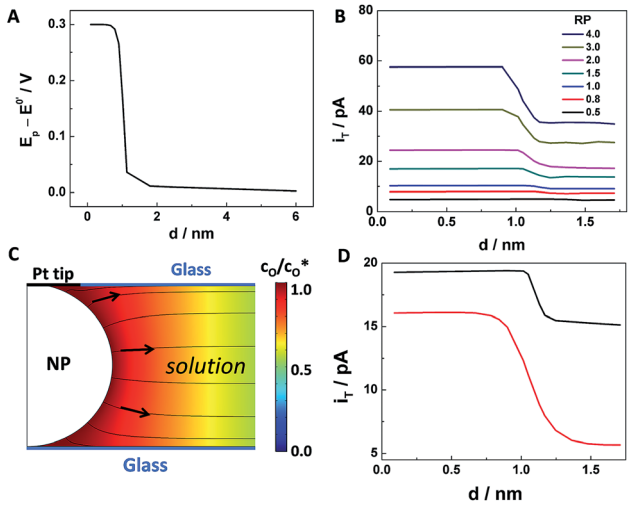

Fig. 6 Numerical simulations of tunnelling mode SECM responses at NPs attached to an insulating support. $r_p = 50$ nm, $a = 30$ nm. $E_T = E^0 + 0.3$ V. (A) E_P–d curve; diffusion-controlled ET at both the tip and NP. (B) i_T–d curves show the transition from feedback to tunnelling for Nernstian ET at different RP values. (C) The 2D concentration distribution of the oxidized species. $d = 1$ nm. The thin lines and arrows represent the flux of the oxidized species in solution. (D) The effect of finite ET kinetics on tunnelling SECM i_T–d curve. Black curve – Nernstian ET; red curve–$k^0 = 0.01$ cm s^{-1}.

as a part of the tip electrode, and the same oxidation process occurs at its entire surface.

The effect of finite ET kinetics on the i_T–d dependence in the tunnelling regime can be seen by comparing the red ($k^0 = 0.01$ cm s^{-1}) and black (Nernstian ET reaction) curves in Fig. 6D. The lower tip current in the red curve just before the onset of tunnelling (*e.g.*, at $d = 2$ nm) corresponds to the smaller positive feedback current (*cf.* Fig. 4C). At smaller d, the tip current in the red curve remains lower due to the higher interfacial ET resistance, and at $E_T = E^0 + 0.3$ V, its plateau value is below the diffusion limit.

The above theory was used to fit an experimental current–distance curve obtained with the Fc mediator at an Au NP (Fig. 7). The onset of tunneling is evident from the sharp increase in the slope of this curve for $d \approx 2.5$ nm. At larger separation distances, the experimental data (symbols) was fitted to the theory for the bipolar SECM feedback (blue line), while the tunnelling model (red line) fits well the experimental i_T–d curve at shorter distances. The tunnelling constant, $\beta = 1.0$ Å^{-1} (eqn (19) in Appendix) was extracted from the fit. Clearly, the i_T–d curve in the tunnelling region does not agree with the theory based on bipolar SECM feedback (dashed blue line).

Probing single NP catalysis using the tunnelling mode of SECM

From Fig. 4C, one can see that only a fast faradaic process occurring at an unbiased nanoparticle can produce significant positive feedback. The open-circuit NP potential imposed by dissolved redox species cannot be sufficiently far from the E^0 value to drive a kinetically slow heterogeneous process, such as the

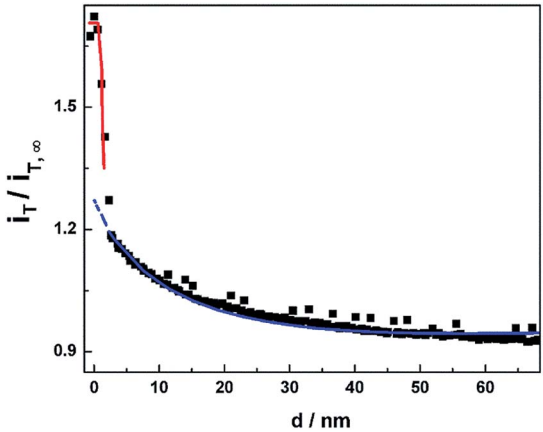

Fig. 7 Transition from the feedback to tunnelling SECM response. Experimental (symbols) current–distance curve obtained with a 42 nm-radius Pt tip approaching a 50 nm-radius Au NP and theoretical curves simulated for the SECM feedback (blue line) and tunnelling (red line). The solution contained 1 mM Fc and 0.1 M KCl. $E_T = 400$ mV *vs.* Ag/AgCl.

hydrogen oxidation reaction (HOR), at an Au NP. Accordingly, the tip current decreased with decreasing d in Fig. 8 that was obtained with the hydrogen evolution reaction (HER) at the Pt tip. The sharp increase in i_T can be seen at short separation distances, at which E_P approached the E_T value (−700 mV *vs.* Ag/AgCl), and HER occurred at the NP surface. It is interesting to notice that the d value of ~2–3 nm corresponding to the onset of electron tunnelling and $\beta = 1.0$ Å^{-1} are very similar for HER and Fc oxidation (*cf.* Fig. 7 and 8A).

The feedback and tunnelling portions of the current–distance curve in Fig. 8A were fitted to the theory using the same value of the apparent standard rate constant for HOR (blue line) and HER (red line) at the Au NP, $k^0 = 0.01$ cm s^{-1}. The overpotential was evaluated as $E_T - E_{RHE} = E_T + E^0_{Ag/AgCl} - (E^0_{RHE} - 0.059 \times pH) = -0.7$ V + 0.1976 V − (0–0.059 × 2.3) = −0.364 V. In this way, heterogeneous kinetics at the unbiased NP can be evaluated from both bipolar feedback and tunnelling responses. Another possibility is to perform voltammetry at the NP surface, as shown in Fig. 8B. The steady-state voltammograms of HER at the Pt tip in the bulk solution (curve 1 in Fig. 8B) and within the tunnelling distance from the Au NP (curve 2) were obtained with the much smaller tip and NP than those used in Fig. 8A ($r_p = 10$ nm, $a = 18$ nm). The onset of current in curve 1 is ~0.5 V more positive than that in curve 2, due to the difference between HER overpotentials at Pt and Au. This approach enables probing catalytic reactions at a single NP without attaching it to the electrode surface.

The above findings can also be useful for interpreting the results of electrochemical collision experiments. For instance, our recent experiments with a single Ir oxide NP trapped inside a conductive (carbon) nanocavity showed the frequency of collision events producing spikes of catalytic current (due to the oxidation of H_2O_2 at the IrO_x NP) about six orders of magnitude lower that the collision frequency predicted by the Einstein's formula.[23] The NPs in a thin liquid layer adjacent to the solid surface were shown to undergo numerous adsorption/desorption cycles,[24] and it was suggested that because of the surface

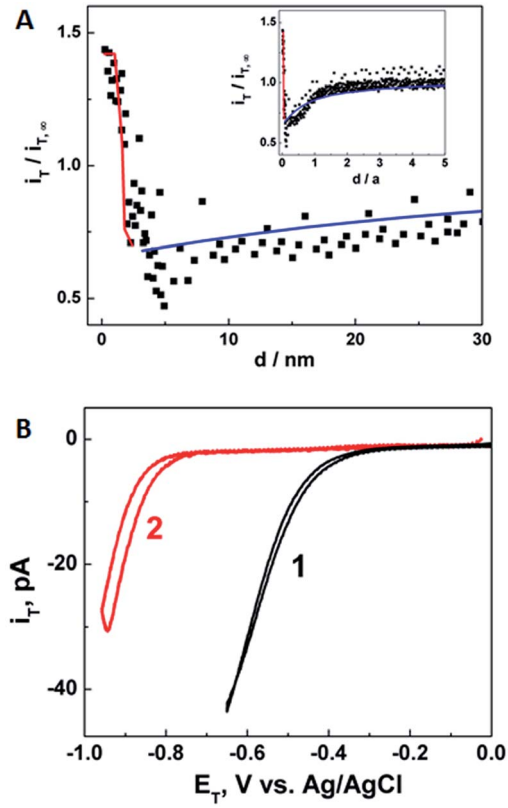

Fig. 8 Probing HOR and HER at a single AuNP using a SECM operating in the feedback and tunnelling modes. (A) The experimental current–distance curve obtained with a 42 nm-radius Pt tip approaching a 50 nm-radius Au NP in solution containing 5 mM $HClO_4$ and 0.1 M KCl (symbols) and the corresponding theory for the feedback (blue line) and tunnelling (red line) modes. The apparent standard rate constant, $k^0 = 0.01$ cm s^{-1} was used for simulating both feedback and tunnelling processes. $E_T = -700$ mV *vs.* Ag/AgCl. The inset shows the long-range current distance curve. (B) Voltammograms of HER recorded at the same Pt tip in the bulk solution (1) and within the tunnelling distance from the AuNP (2). $r_p = 10$ nm, $a = 18$ nm.

heterogeneity, the NPs can be either weakly or strongly bound at different surface sites.[25] One can hypothesize that measurable current spikes occur during relatively rare strong binding events, while the weak binding events are "silent" collisions, producing no electrochemical signal. From the results discussed in this paper, one can infer that a NP approaches the electrode surface to within the tunneling distance (<2 nm) only during the infrequent, strong binding events.

Electron tunnelling between the SECM tip and a metal nanorod

The tunnelling mode of SECM can be useful for probing electrochemical processes at non-spherical nanostructures such as nanorods or two-dimensional catalytic nanoflakes. The faradaic current at a relatively large particle, *e.g.*, a micrometre-long nanorod (and the diffusion limiting current to it) can be orders

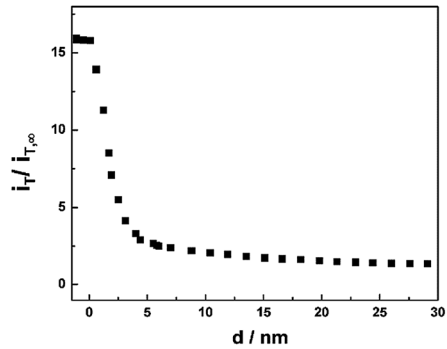

Fig. 9 Experimental current–distance curve obtained with a 30 nm-radius carbon tip approaching a 370 nm diameter Au–Pt nanorod. The solution contained 1 mM Fc and 0.1 M KCl. $E_T = 400$ mV *vs.* Ag/AgCl. The nanorod length is 1–2 μm.

of magnitude higher than that at 10–50 nm radius NPs discussed above. The overall charge-transfer process in Fig. 2 includes two steps, *i.e.* the electron tunneling between the tip and the NP and the electrochemical reaction at the NP surface, each of which can be rate limiting. Thus, faradaic reaction is likely to be the rate-limiting step at a small NP, and tunnelling at a large one.

Approaching a nanorod is technically harder than a spherical NP. In the above experiments, the top of a spherical NP was significantly above the substrate plane, allowing the Pt tip to approach it without the insulating sheath touching the underlying glass surface. However, a significant thickness of the insulating sheath (*e.g.*, RG = 10) prevents a Pt tip from coming very close to the surface of a relatively long nanorod. To overcome this problem, carbon tips with a very thin quartz insulating sheath (*e.g.*, RG ≈ 1.1)[18] were used in these experiments. In Fig. 9, the transition from feedback to tunnelling starts at a somewhat longer distance, ~3–4 nm, and the plateau tunnelling current is as high as $16i_{T,\infty}$. Additional experiments and simulations are needed to clarify whether this value is equal to the diffusion limiting current of Fc to the NP.

SECM experiments at bimetallic nanorods can potentially be useful for investigating the effect of the substrate material (*e.g.*, Au *vs.* Pt) on electrochemical tunneling. The rate of the heterogeneous reaction at the nanorod/solution interface and the diffusion current of the redox species to the rod surface should be the same whether the tip is positioned over the Au or Pt portion. In contrast, the tunneling currents at Au and Pt may be different due to different work functions and contact electrification of metal surfaces.[26] Thus, the tunneling mode of SECM may be suitable for high-resolution surface reactivity mapping of heterogeneous catalysts. These experiments are currently underway in our laboratory.

Conclusions

Although long-distance electron transfer between the NPs and underlying electrode surface is ubiquitous in electrochemical systems, probing this process as a function of the separation distance is challenging. Here, we developed

a tunnelling mode of SECM that allows one to control and vary d with the sub-nm precision. By fitting experimental current–distance curves to a simple approximate model, one can describe the transition from the bipolar NP response producing SECM feedback to electron tunnelling between the tip and NP. This sharp transition, occurring over the tip displacement of ~1 nm, involves the change in E_P from the open circuit value to that determined by the tip potential.

The developed methodology allows one to investigate heterogeneous processes occurring at a single NP without making an ohmic contact with it. The values of the heterogeneous rate constant at the NP and the tunneling constant were obtained by analysis of the current–distance curves. Steady-state voltammograms at a single NP were recorded without attaching it to the electrode surface. These approaches can enable studying the effects of nanoparticle size and geometry on electrocatalytic activity in real-world application environments. In addition to metal NPs, other nanostructures, such as metal nanorods and 2D catalytic nanoflakes, can be addressed by the SECM tip in the tunnelling mode. An important question is whether the tunnelling response depends on the nature of the approached nanostructure; such a dependence would enable high-resolution reactivity mapping in the tunnelling SECM mode.

Appendix: mathematical models

Feedback mode

In the feedback mode, the tip is held at a potential at which the oxidation of the solution redox species is diffusion limited, and the generated oxidized species get reduced at the unbiased NP *via* a bipolar electrochemical process (Fig. 1B). The diffusion and electron tunnelling problems were formulated and solved with the "Transport of Diluted Species" and "Electric Currents" modules of COMSOL 5.2a. The 2-D axisymmetric geometry was used (Scheme 1), with two simulation domains for the solution and Au NP. The geometric parameters a, r_g, r_p and d represent the tip electrode radius, glass radius, NP radius and the tip-nanoparticle separation distance, respectively, and the solution contains reduced (R) and oxidized (O) forms of the redox species. The stationary diffusion equation was used for both reduced (R) and oxidized (O) forms of the redox species in solution:

$$\frac{\partial^2 c_i}{\partial r^2} + \frac{1}{r}\frac{\partial c_i}{\partial r} + \frac{\partial^2 c_i}{\partial z^2} = 0, i = O, R;\ 0 \le r < r_s, -l < z < d + 2r_p. \quad (1)$$

The concentrations of the R and O species in the solution are:

$$c_O = 0,\ c_R = 1\ \text{mM};\ 0 \le r < r_s,\ -l < z < d + 2r_p,\ \text{(initial conditions)} \quad (2)$$

and

$$c_O = 1\ \text{mM},\ c_R = 0;\ 0 \le r < a,\ z = 0;\ \text{(tip surface)}. \quad (3)$$

At the nanoparticle surface, the ionic fluxes, J_O and J_R, are defined by the Butler–Volmer equation:

$$J_O = k^0 c_R \exp\left[(1-\alpha)\frac{F}{RT}\left(E_p(r,z) - E^{0'}\right)\right] - k^0 c_O \exp\left[-\alpha\frac{F}{RT}\left(E_p(r,z) - E^{0'}\right)\right];$$

$$J_R = -J_O;\ \ 0 \le r \le r_p, z = d + r_p \pm \sqrt{r_p{}^2 - r^2};\ \ (\text{NP surface}) \tag{4}$$

where $J_O = -D_O \nabla c_O$ and $J_R = -D_R \nabla c_R$ are the fluxes of redox species, k^0 and $E^{0'}$ are the standard rate constant and formal potential, F is the Faraday constant, R and T are the gas constant and temperature, and α is the transfer coefficient ($\alpha = 0.5$). $E_P(r, z)$ is the NP surface potential. By considering the bipolar nanoparticle as an infinite series of the elementary electrical nodes,[27] the potential distribution, $V_P(r, z)$ within the NP domain and the electric current density at the NP surface (FJ_O) would follow Ohm's law:

$$i = -\sigma \nabla V_p(r, z),$$

$$0 \le r \le r_p, d + r_p - \sqrt{r_p{}^2 - r^2} \le z \le d + r_p + \sqrt{r_p{}^2 - r^2};\ \ (\text{within NP}) \tag{5}$$

where i is the local current density and σ is the metal conductivity. At the nanoparticle surface, $V_p(r, z) = E_P(r, z)$ in eqn (4). Other boundary conditions are given by

$c_O = 0$, $c_R = 1$ mM; $r_g \le r < r_s$, $z = -l$; $r = r_s$, $-l < z < d + 2r_p$ (simulation space limits) (6)

$$J_R = J_O = 0;\ a \le r < r_g,\ z = 0,\ (\text{glass insulator}) \tag{7}$$

$$J_R = J_O = 0;\ 0 \le r < r_s,\ z = d + 2r_p,\ (\text{insulating substrate}) \tag{8}$$

$$J_R = J_O = 0;\ r = r_g,\ -l < z < 0,\ (\text{glass insulator}). \tag{9}$$

The tip current is then obtained by surface integrating of the flux (J_O) at the tip surface,

$$i_T = 2\pi F \int_0^a J_O r dr;\ \ 0 \le r \le a, z = 0;\ \ (\text{tip surface}). \tag{10}$$

When the tip is positioned far away from the NP, the steady-state diffusion limiting current is

$$i_{T,\infty} = 4nFDca. \tag{11}$$

Tunnelling mode

The stationary diffusion equation was used for both reduced (R) and oxidized (O) forms of redox species in solution:

$$\frac{\partial^2 c_i}{\partial r^2} + \frac{1}{r}\frac{\partial c_i}{\partial r} + \frac{\partial^2 c_i}{\partial z^2} = 0, i = O, R;\ \ 0 \le r < r_s, -l < z < d + 2r_p. \tag{12}$$

The initial concentration of the oxidized and reduced forms in the solution are

$$c_O = 0,\ c_R = 1\ \text{mM};$$

$$0 \le r < r_s,\ -l < z < d + 2r_p;\ \text{(initial condition)} \tag{13}$$

As the tip current is diffusion-controlled,

$$c_O = 1\ \text{mM},\ c_R = 0\ \text{mM};\ 0 \le r < r_s,\ z = 0;\ \text{(tip surface)} \tag{14}$$

In the solution domain, other boundary conditions are given by

$$c_O = 0,\ c_R = 1\ \text{mM};\ r_g = r < r_s,\ z = -l;\ r = r_s,\ -l < z < d + 2r_p\ \text{(simulation space limits)} \tag{15}$$

$$J_R = J_O = 0;\ a < r < r_g,\ z = 0,\ \text{(glass insulator)} \tag{16}$$

$$J_R = J_O = 0;\ 0 \le r < r_s,\ z = d + 2r_p,\ \text{(insulating substrate)} \tag{17}$$

$$J_R = J_O = 0;\ r = r_g,\ -l \le z \le 0,\ \text{(glass insulator)} \tag{18}$$

The tunnelling resistance is a function of the separation distance, d[27]

$$R_t = \frac{d}{C_1} e^{\beta d} \tag{19}$$

where C_1 and β are constants that depend on the experimental conditions. β is typically $\sim 1.0 \times 10^{-10}$ m^{-1}, and $C_1 = 10^{-14}$ m Ω^{-1}.[11] The tip potential (E_T) drops across the tunnelling resistance (E_t), and the AuNP/solution interface (E_P), and the later component drives the ET process, according to the Butler–Volmer equation:

$$\begin{aligned} &J_O = k^0 c_R \exp\left[(1-\alpha)\frac{F}{RT}\left(E_p - E^{0'}\right)\right] - k^0 c_O \exp\left[-\alpha\frac{F}{RT}\left(E_p - E^{0'}\right)\right], \\ &J_R = -J_O;\ \ 0 \le r \le r_p,\ \ z = d + r_p \pm \sqrt{r_p^2 - r^2};\ \ (\text{NP surface}). \end{aligned} \tag{20}$$

The potential drop within the Au NP can be ignored because its resistance is too small compared to either tunnelling resistance or electron transfer resistance. Thus, the E_P is essentially constant over the NP surface. The total current (i_P) at the NP can be obtained by integrating the O flux at the particle surface:

$$i_P = F \iint J_O \mathrm{d}S. \tag{21}$$

The tunnelling resistance connects the tip and the nanoparticle, and thus the tip potential can be expressed as:

$$E_T = E_t + E_P = R_t \times i_P + E_P. \tag{22}$$

Therefore, by solving eqn (19)–(22) together, the E_P and i_P can be calculated at various separation distance values. The measured tip current additionally includes the diffusion current of O to the tip surface largely blocked by the NP:

$$i_T = i_P + 2\pi F \int_0^a J_O r dr; 0 \le r \le a, \quad z = 0 \text{ (tip surface)}. \tag{23}$$

Conflicts of interest

There are no conflicts to declare.

Acknowledgements

The support of this work by the U.S. Department of Energy, Basic Energy Sciences under grant no. DE-SC0017603 (development of the tunneling mode of SECM) and National Science Foundation (CHE-1763337; probing electrochemical processes at single NPs) is gratefully acknowledged. We thank Prof. Michael D. Ward, Yang Wu and Xiao Zhong (New York University) for providing the nanorods used in Fig. 9, and Keke Hu for preparing carbon nanoelectrodes.

Notes and references

1 *Metal nanoparticles: synthesis, characterization, and applications*, ed. D. L. Feldheim and C. A. Foss, Marcel Dekker, New York, 2002; M.-C. Daniel and D. Astruc, *Chem. Rev.*, 2004, **104**, 293; R. W. Murray, *Chem. Rev.*, 2008, **108**, 2688; F. P. Zamborini, L. Bao and R. Dasari, *Anal. Chem.*, 2012, **84**, 541; S. E. Kleijn, S. C. Lai, M. T. Koper and P. R. Unwin, *Angew. Chem., Int. Ed.*, 2014, **53**, 3558; R. M. Anderson, D. F. Yancey, L. Zhang, S. T. Chill, G. Henkelman and R. M. Crooks, *Acc. Chem. Res.*, 2015, **48**, 1351

2 A. E. Gerdon, D. W. Wright and D. E. Cliffel, *Angew. Chem., Int. Ed.*, 2006, **45**, 594; A. B. Chinen, C. M. Guan, J. R. Ferrer, S. N. Barnaby, T. J. Merkel and C. A. Mirkin, *Chem. Rev.*, 2015, **115**, 10530.

3 X. Huang, S. Neretina and M. A. El-Sayed, *Adv. Mater.*, 2009, **21**, 4880; *Nanomaterials for Fuel Cell Catalysis*, ed. K. I. Ozoemena and S. Chen, Springer, 2016; W. Albrecht, J. E. S. van der Hoeven, T.-S. Deng, P. E. de Jongh and A. van Blaaderen, *Nanoscale*, 2017, **9**, 2845.

4 G. Yang, C. Zhu, D. Du, J. Zhu and Y. Lin, *Nanoscale*, 2015, **7**, 14217; M. Pumera, Z. Sofer and A. Ambrosi, *J. Mater. Chem. A*, 2014, **2**, 8981; M. Pumera and A. H. Loo, *Trends Anal. Chem.*, 2014, **61**, 49; A. B. Kaul, *J. Mater. Res.*, 2014, **29**, 348; K. Krishnamoorthy, G. K. Veerasubramani and S. J. Kim, *Gram Sci. Adv. Mater.*, 2015, **7**, 1247.

5 J. Kim, B. K. Kim, S. K. Cho and A. J. Bard, *J. Am. Chem. Soc.*, 2014, **136**, 8173; C. M. Hill, J. Kim and A. J. Bard, *J. Am. Chem. Soc.*, 2015, **137**, 11321.

6 E. Kätelhön, E. E. L. Tanner, C. Batchelor-McAuley and R. G. Compton, *Electrochim. Acta*, 2016, **199**, 297.

7 J. Zhao, S. Sun, L. Swartz, S. Riechers, P. Hu, S. Chen, J. Zheng and G.-y. Liu, *J. Phys. Chem. Lett.*, 2015, **6**, 4986; C. Gupta, R. M. Walker, S. Chang, S. R. Fischer, M. Seal, B. Murmann and R. T. Howe, *J. Phys. Chem. C*, 2017, **121**, 15085.

8 G. Chen, R. Perez-Garcia, J. Danglad-Flores and H. Riegler, *J. Phys. Chem. Lett.*, 2017, **8**, 6094.
9 J. Zhao, C. R. Bradbury, S. Huclova, I. Potapova, M. Carrara and D. J. Fermin, *J. Phys. Chem. B*, 2005, **109**, 22985.
10 J. Chazalviel and P. Allongue, *J. Am. Chem. Soc.*, 2010, **133**, 762.
11 E. Kätelhön and R. G. Compton, *ChemElectroChem*, 2015, **2**, 64.
12 T. Sun, Y. Yu, B. J. Zacher and M. V. Mirkin, *Angew. Chem., Int. Ed.*, 2014, **53**, 14120; Y. Yu, T. Sun and M. V. Mirkin, *Anal. Chem.*, 2015, **87**, 7446.
13 A. J. Bard, F.-R. F. Fan, J. Kwak and O. Lev, *Anal. Chem.*, 1989, **61**, 132.
14 H. Xiong, J. D. Guo and S. Amemiya, *Anal. Chem.*, 2007, **79**, 2735.
15 P.-Y. Blanchard, T. Sun, Y. Yu, Z. Wei, H. Matsui and M. V. Mirkin, *Langmuir*, 2016, **32**, 2500; M. V. Mirkin, T. Sun, Y. Yu and M. Zhou, *Acc. Chem. Res.*, 2016, **49**, 2328.
16 M. S. Davies Wykes, J. Palacci, T. Adachi, L. Ristroph, X. Zhong, M. D. Ward, J. Zhang and M. J. Shelley, *Soft Matter*, 2016, **12**, 4584.
17 P. Sun and M. V. Mirkin, *Anal. Chem.*, 2006, **78**, 6526.
18 Y. Yu, Y. Gao, K. Hu, P.-Y. Blanchard, J.-M. Noël, T. Nareshkumar, K. L. Phani, G. Friedman, Y. Gogotsi and M. V. Mirkin, *ChemElectroChem*, 2015, **2**, 58; R. Chen, K. Hu, Y. Yu, M. V. Mirkin and S. Amemiya, *J. Electrochem. Soc.*, 2016, **163**, H3032.
19 J. H. Bae, R. F. Brocenschi, K. Kisslinger, H. L. L. Xin and M. V. Mirkin, *Anal. Chem.*, 2017, **89**, 12618.
20 Y. D. Jin, X. F. Kang, Y. H. Song, B. L. Zhang, G. J. Cheng and S. J. Dong, *Anal. Chem.*, 2001, **73**, 2843.
21 C. Wei, A. J. Bard and M. V. Mirkin, *J. Phys. Chem.*, 1995, **99**, 16033; Y. Wang, J. Velmurugan and M. V. Mirkin, *Isr. J. Chem.*, 2010, **50**, 291; R. Chen, N. Nioradze, P. Santhosh, Z. Li, S. P. Surwade, G. J. Shenoy, D. G. Parobek, M. A. Kim, H. Liu and S. Amemiya, *Angew. Chem., Int. Ed.*, 2015, **54**, 15134.
22 J. Velmurugan, P. Sun and M. V. Mirkin, *J. Phys. Chem. C*, 2009, **113**, 459.
23 M. Zhou, Y. Yu, K. Hu, H. Xin and M. V. Mirkin, *Anal. Chem.*, 2017, **89**, 2880.
24 M. J. Skaug, J. Mabry and D. K. Schwartz, *Phys. Rev. Lett.*, 2013, **110**, 256101.
25 S. W. Chee, Z. Baraissov, N. D. Loh, P. T. Matsudaira and U. Mirsaidov, *J. Phys. Chem. C*, 2016, **120**, 20462.
26 S. W. Thomas, S. J. Vella, M. D. Dickey, G. K. Kaufman and G. M. Whitesides, *J. Am. Chem. Soc.*, 2009, **131**, 8746; P. Peljo, J. A. Manzanares and H. H. Girault, *Langmuir*, 2016, **32**, 5765.
27 A. Oleinick, J. Yan, B. Mao, I. Svir and C. Amarore, *ChemElectroChem*, 2016, **3**, 487.

